condensed matter

MDPI

*Article*

# Structural, Magnetic, and Electrical Properties and Magnetoresistance of Monovalent K-Substituted $La_{0.7}Ba_{0.3-x}K_xMnO_3$ ($x$ = 0 and 0.04) Manganite

**Amirah Zahrin, Nurul Atiqah Azhar, Norazila Ibrahim and Zakiah Mohamed ***

School of Physics and Material Studies, Faculty of Applied Sciences, Universiti Teknologi MARA, Shah Alam 40450, Selangor Darul Ehsan, Malaysia
* Correspondence: zakiah626@uitm.edu.my

**Abstract:** The effects of $K^+$ substitution at the Ba-site on the structural, magnetic, and electrical properties and magnetoresistance (MR) of $La_{0.7}Ba_{0.3-x}K_xMnO_3$ ($x$ = 0 and 0.04) manganites prepared via the solid-state method were investigated. Rietveld refinement of X-ray diffraction data confirmed that both samples were crystallized in the rhombohedral structure with the $R3\bar{c}$ space group. In addition, the unit cell volume, $V$, and the average grain size also increased with $K^+$ ions. Magnetization versus applied field ($M$–$H$) measurement was carried out, and the saturation magnetization ($M_s$) was found to increase from 1.81 $\mu_B$/f.u. ($x$ = 0) to 4.11 $\mu_B$ /f.u. ($x$ = 0.04), implying that $K^+$ ions strengthened the ferromagnetic (FM) interaction. Furthermore, the metal–insulator transition temperature, $T_{MI}$, increased from 257 K ($x$ = 0) to 271 K ($x$ = 0.04). The observed behaviour may be related to the enhancement of double-exchange (DE) interaction due to the increase in Mn-O-Mn bond angle and electronic bandwidth ($W$), favouring the increasing rate of the $e_g$ electron hopping process. The fitting of the electrical resistivity data in the metallic region describes the significance of residual resistivity, electron–electron and electron–magnon scattering processes to elucidate the electronic transport properties. Within the insulating region, variable range hopping (VRH) and small polaron hopping (SPH) models are proposed to describe the conduction mechanism.

**Keywords:** magnetic materials; X-ray diffraction; manganites; electrical properties; magnetic properties



**Citation:** Zahrin, A.; Azhar, N.A.; Ibrahim, N.; Mohamed, Z. Structural, Magnetic, and Electrical Properties and Magnetoresistance of Monovalent K-Substituted $La_{0.7}Ba_{0.3-x}K_xMnO_3$ ($x$ = 0 and 0.04) Manganite. *Condens. Matter* **2022**, *7*, 51. https://doi.org/10.3390/condmat7030051

Academic Editor: Víctor Manuel García Suárez

Received: 21 July 2022
Accepted: 17 August 2022
Published: 24 August 2022



## 1. Introduction

In recent years, increasing attention has been given to perovskite manganite with the general formula of $La_{1-x}A_xMnO_3$ (A = divalent elements such as Ca, Sr, and Ba) due to its unique feature of a phase diagram as a result of the complicated interplay between its charge, orbital ordering, spin, and lattice degrees of freedom [1]. The utmost traits of manganites include their multiferroic and magneto-transport properties, which can be tuned by external stimuli (such as magnetic field, pressure, X-rays radiation, injection of electrical current, etc.) or the substitution/addition of elements to improve the remarkable phenomena of magnetoresistance (MR) effect, where the electrical resistivity is reduced by orders of magnitude under the presence of an external magnetic field [2]. Manganites exhibiting high MR effects are extensively explored as they present opportunities for potential technological applications, such as magnetic sensors [3,4], non-volatile memory-based elements [5], and spintronic-based devices [6]. Interestingly, lanthanum perovskite manganite has also been recently proposed as a novel Dirac half-metal [7] material due to the large spin polarization and low energy consumption compared to conventional electronics. Pertaining to these remarkable findings, further $LaMnO_3$ studies are essential as they open the possibility of realizing colossal MR behaviours in manganite systems and emerging spintronic-based applications.

In perovskite manganites, the transport properties are mainly governed by Zener's double-exchange (DE) mechanism involving the hopping of charge carriers from neigh-

bouring Mn sites via $O^{2-}$ ions in a $Mn^{3+}$-$O^{2-}$-$Mn^{4+}$ network [8]. According to Zener's model, $e_g$ itinerant electrons can easily hop from the $Mn^{3+}$ site to the $Mn^{4+}$ site if the spins of manganese ions are aligned in parallel and are ferromagnetically coupled [8]. Further investigations have confirmed that the strength of the DE mechanism is also influenced by the lattice distortion effects due to the substitution of cations at the A-site, which induces changes in the average ionic radius (<$r_A$>), the Mn-O–Mn bond angle, as well as the Mn–O bond length [9–11]. These parameters are also regarded as controlling factors behind the occurrence of A-site disorder ($\sigma^2$), tolerance factor ($\tau_G$), electronic bandwidth (W), and many other phenomena in a perovskite system. According to previous studies, the introduction of a large A-site cation, such as $Ag^+$ in $La_{0.7}Ca_{0.3-x}Ag_xMnO_3$ [12] and $K^+$ in $La_{1-x}K_xMnO_3$ [3], increases the bond angle and reduces the bond length. Consequently, the transfer of charge carriers between Mn ions via oxygen becomes easier and therefore facilitates the DE interaction. Furthermore, Zaidi et al. also presented the electrical behaviour study of $La_{0.67}Pb_{0.33-x}Na_xMnO_3$ [13] manganites. The study attributed the decrease in $T_{MI}$ to the reduction in <$r_A$> as a result of smaller $Na^+$ substitution, which leads to the narrowing of the bandwidth ($W$) and in turn reduces the mobility of the $e_g$ conduction electrons. In general, the influence of A-site substitution on transport properties depends on the size of doped ions and the degree of lattice distortion related to the modifications in bond length and bond angle.

Apart from structural modification due to the replacement of different ionic radii, the substitution of monovalent ions (e.g., Li, Na, K, and Ag) is also interesting, owing to its ability to induce twice more $Mn^{4+}$ ions with $x$ substitution compared to divalent ions [9,10]. In this case, only a small doping $x$ concentration is required to induce the optimum ratio of $Mn^{3+}/Mn^{4+}$ at 0.33, where the magnetotransport properties are the most prominent [14]. Potassium ($K^+$) exhibits the largest ionic radius among other monovalent elements and is often substituted in La-based manganite compounds [6,15–18]. Interestingly, the substitution of $K^+$ has been reported to enhance the DE process and the magnetic properties by increasing the value of metal–insulator transition temperature, $T_{MI}$, and Curie temperature, $Tc$, in several manganites, such as $La_{1-x}K_xMnO_3$ [3,17], $La_{0.7}Ca_{0.3-x}K_xMnO_3$ [19], and $Pr_{0.8}Na_{0.2-x}K_xMnO_3$ [20]. Furthermore, $K^+$ has also been reported to destabilize the charge-ordering (CO) state in $Pr_{0.75}Na_{0.25-x}K_xMnO_3$ and drive the system towards ferromagnetic–metallic (FMM) behaviour [21]. Meanwhile, Jeddi et al. found that with the increase in the $K^+$ fraction $x$ in $Nd_{0.6}Sr_{0.4-x}K_xMnO_3$ [9], $T_C$ and the $T_{MI}$ decrease with a corresponding rise in the MR effect. Therefore, the substitution of $K^+$ is expected to promote rich functionalities in the transport system of perovskite manganites.

In the present work, the effect of $K^+$ substitution in $La_{0.7}Ba_{0.3-x}K_xMnO_3$ is elaborated to investigate its structural, magnetic, and electrical transport properties. $La_{1-x}Ba_xMnO_3$ manganite is an extensively studied compound that exhibits an FM state at $x > 0.25$ above room temperature while also displaying a long range of FM ordering that is highly desired from the viewpoint of technological applications [1,22–24]. In this regard, $La_{0.7}Ba_{0.3}MnO_3$ manganite is selected as the parent compound as it exhibits $T_C$ and $T_{MI}$ close to room temperature [25,26]. To our knowledge, neither magnetic nor electrical properties have been investigated in K-substituted $La_{0.7}Ba_{0.3-x}K_xMnO_3$. Different theoretical models have been used to explain the charge conduction mechanism responsible for the temperature-dependent resistivity graph.

## 2. Results and Discussion

### *2.1. Structural Properties*

#### 2.1.1. X-ray Diffraction (XRD) Analysis

Figure 1 displays the room temperature X-ray diffraction (XRD) pattern along with the Rietveld refinement for $La_{0.7}Ba_{0.3-x}K_xMnO_3$ ($x$ = 0 and 0.04). Both samples exhibit a single phase and are indexed in a rhombohedral structure ($a = b \neq c$) with the $R3\bar{c}$ space group. The sharpness of intensity peaks indicates the formation of samples with high crystallinity [1,27], and the location of peaks was also consistent with the previous studies

of $La_{0.7}Ba_{0.3}MnO_3$ [27,28]. A minor additional peak denoted by the (*) symbol in Figure 1 associated with the $Mn_3O_4$ phase was detected for sample $x = 0.04$ at angle $2\theta = 36.1^\circ$ using X'pert High Score Plus software (reference code: 00-024-0734). Furthermore, the small difference between the observed and calculated data (blue line) suggested a good fitting quality, which can also be seen by the small value of the goodness factor ($\chi^2 \sim 1$), as shown in Table 1.

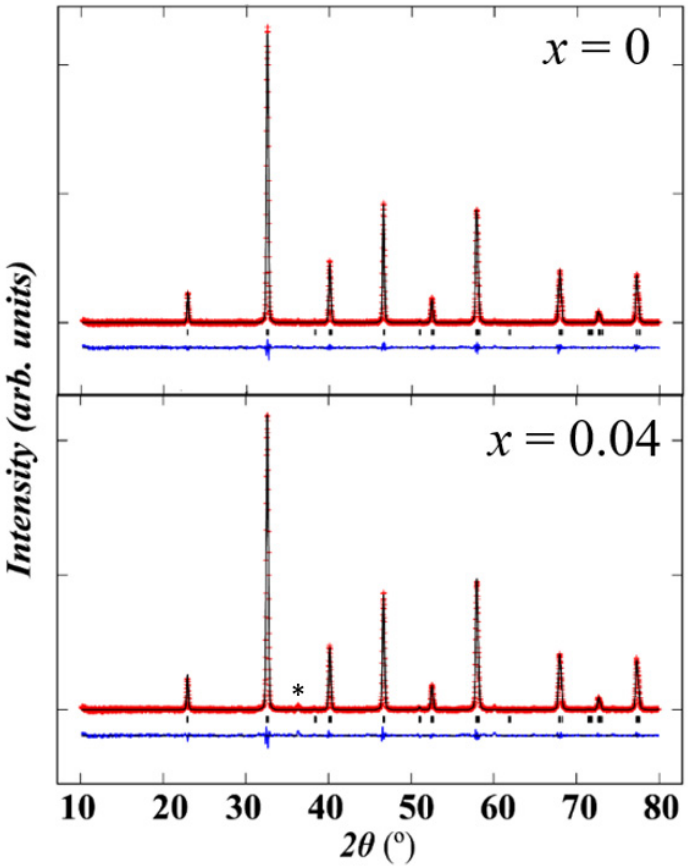


**Figure 1.** Rietveld refinement of the XRD patterns for $La_{0.7}Ba_{0.3-x}K_xMnO_3$ ($x = 0$ and 0.04). The solid red line represents the observed data, the black line corresponds to the calculated data, whilst the blue lines correspond to the difference between the observed and calculated data. Tick marks (vertical) indicate the allowed Bragg position. The presence of minor additional $Mn_3O_4$ peak was indicated by the "*" symbol.

The refined lattice parameters, bond angle, and bond length are summarized in Table 1. It can be seen in Figure 2a that the structural parameters *a* and *b* increased from 5.5344 Å ($x = 0$) to 5.5405 Å ($x = 0.04$), while *c* slightly decreased from 13.527 Å ($x = 0$) to 13.524 Å ($x = 0.04$) with $K^+$ substitution. In addition, the unit cell volume, *V*, increased as $K^+$ was substituted from 358.81 $(Å)^3$ ($x = 0$) to 359.53 $(Å)^3$ ($x = 0.04$). The observed behaviour is justified due to the fact that larger $K^+$ (1.55 Å) is substituted into smaller $Ba^{2+}$ (1.47 Å) ions [16], which possibly induced the lattice expansion in both *a* and *b* directions, thereby leading to the increase in unit cell volume. Hence, the increase in average ionic radius at A-site, $< r_A >$ was expected (Table 1) and subsequently gave rise to the lattice-distortion effect, which can be characterized by the A-site disorder ($\sigma^2$) parameter expressed using the following equation [16]:

$$\sigma^2 = \sum x_i r_i^2 - < r_A >^2 \quad (1)$$

where $x_i$ and $r_i^2$ is the fractional occupancy of A-site ions and ionic radius. The increasing value of $\sigma^2$ from 1.3548 $Å^2$ ($x = 0$) to 1.4932 $Å^2$ ($x = 0.04$), as shown in Table 1, indicates that $K^+$ increases the disorder and the lattice distortion due to the mismatch in the cation size.

**Table 1.** Lattice parameters, unit cell volume ($V$), and goodness of fit ($\chi^2$) obtained from Rietveld refinement for $La_{0.7}Ba_{0.3-x}K_xMnO_3$ ($x$ = 0 and 0.04). $\sigma^2$, $\tau_G$, $W$, and $T_{MI}$ represent the A-site disorder, tolerance factor, electronic bandwidth, and metal–insulator transition temperature, respectively.

| Sample | $x$ = 0 | $x$ = 0.04 |
|---|---|---|
| Crystal structure | Rhombohedral | |
| Space group | $R3\bar{c}$ | |
| $a = b$ (Å) | 5.5344 (18) | 5.5405 (13) |
| $c$ (Å) | 13.527 (9) | 13.524 (5) |
| $V$ (Å)$^3$ | 358.81 (28) | 359.53 (18) |
| Average ionic radius, $<r_A>$ | 1.295 | 1.299 |
| Bond length, <Mn–O> Å | 1.969 (6) | 1.966 (7) |
| Bond angle, <Mn–O–Mn> (°) | 166.6 (0) | 168.7 (4) |
| $\chi^2$ | 1.70 | 2.14 |
| $R_{wp}$ (%) | 6.87 | 7.59 |
| $R_p$ (%) | 4.90 | 5.25 |
| $\sigma^2(\times 10^{-2})$ (Å$^2$) | 1.3548 | 1.4932 |
| $\tau_G$ | 0.9523 | 0.9534 |
| $W$ | 0.0927 | 0.0934 |
| $T_{MI}$ (K) | 257 | 271 |

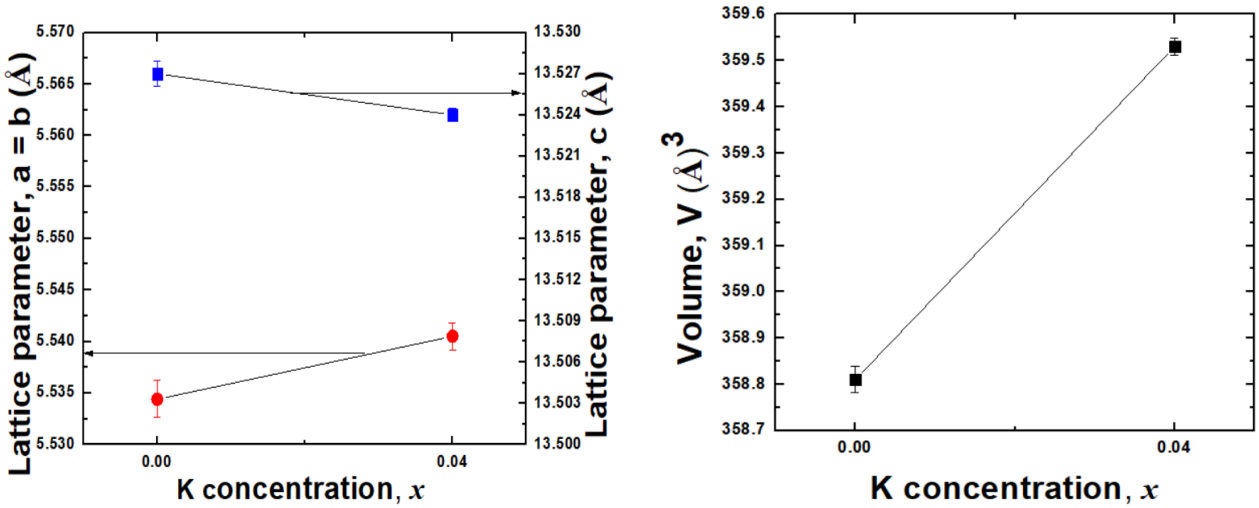


**Figure 2.** Variation of K concentration, $x$, with (**a**) lattice parameter a, b, c, and (**b**) volume in $La_{0.7}Ba_{0.3-x}K_xMnO_3$ ($x$ = 0 and 0.04) sample.

Consequently, lattice distortion may also influence the stability of the perovskite manganite compound governed by Goldschmidt's tolerance factor ($\tau_G$) [29,30]. The tolerance factor was calculated using the followed expression [9,31]:

$$\tau_G = \frac{r_A + r_B}{\sqrt{2}\,(r_B + r_o)} \quad (2)$$

where $r_A$, $r_B$, and $r_O$ represent the average ionic radius at *A*-, *B*-, and *O*- sites. The perovskite manganite compound is considered stable when the $\tau_G$ value lies between the range of 0.89 and 1.2 [32]. Here, it is noted that $\tau_G$ increased from 0.9523 ($x$ = 0) to 0.9534 ($x$ = 0.04), hence implying that the stability of the system increased. Upon $K^+$ substitution, the Mn–O–Mn bond angle increased from 166.6° ($x$ = 0) to 168.7° ($x$ = 0.04), whereas the Mn–O bond length slightly decreased from 1.969 ($x$ = 0) to 1.966 ($x$ = 0.04). The

changes in bond length, as well as bond angle, can further be used to determine the $e_g$ electron bandwidth, $W$, according to the following relation [33]:

$$W = \frac{\cos 1/2\,(\pi - < \mathrm{M_n - O - M_n} >)}{(< \mathrm{M_n - O} >)^{3.5}} \quad (3)$$

The increasing trend of $W$ from 0.0927 ($x$ = 0) to 0.0934 ($x$ = 0.04) suggested that $K^+$ results in the widening of electron bandwidth and the overlapping between the Mn-3d and O-2p orbitals [34]. The increasing stability reflected by high $\tau_G$, as well as larger $W$ as $K^+$ was substituted may enhance the magneto-transport properties, which will be further discussed in the following section.

#### 2.1.2. Scanning Electron Microscope

A scanning electron microscope (SEM) integrated with energy-dispersive X-ray (EDX) spectroscopy revealed more detailed insight into the grain morphology and the elemental distributions in the studied compounds. Figure 3a,b shows the SEM-EDX analysis for $La_{0.7}Ba_{0.3-x}K_xMnO_3$ ($x$= 0 and 0.04). The SEM micrographs revealed that the grains in both compounds are inhomogeneous and exhibit irregular shapes. In addition, the average grain sizes estimated via *ImageJ* software increased from 0.71 µm ($x$ = 0) to 1.34 µm ($x$ = 0.04). The observed increase in grain size is understood to be due to the substitution of larger $K^+$, which is consistent with the increasing trend of unit cell volume in Table 1. Similar behaviour was also reported in another K-substituted compound [15] due to the substitution of a larger doped ion size. EDX analysis was carried out to determine the presence of elements in $La_{0.7}Ba_{0.3-x}K_xMnO_3$ ($x$ = 0 and 0.04). The EDX spectra displayed characteristic peaks of La, Ba, K, Mn, and O elements. No foreign peaks were detected, confirming that both samples contain all the expected chemical elements with no impurities. Moreover, the values of atomic composition (%) obtained from EDX quantitative analysis (Table 2) for all samples were almost equal to their respective stoichiometric values. This result suggests that the investigated samples were appropriately synthesized to form compounds with the desired composition.

### *2.2. Magnetic Properties*

Figure 4 represents the graph of the temperature dependence of the real part of AC susceptibility, $\chi'$, for $La_{0.7}Ba_{0.3-x}K_xMnO_3$ ($x$ = 0 and 0.04) carried out under an AC field of 2 Oe and frequency of 325 Hz. The temperature in which the transition of ferromagnetic to paramagnetic state (FM–PM) occurs, known as Curie temperature ($T_C$), was determined based on the minimum value of $d\chi'/dT$ versus T plot [30,35]. In the present study, no drop in $\chi'$ was observed, implying that both samples possibly exhibit larger $T_C$ above 300 K. This behaviour is coherent with the earlier studies of the parent compound, which reported the value of $T_C$ at 340 K [26] and 348 K [25]. Furthermore, we also note that instead of the drop, a kink in $\chi'$ is observed around 180 K in our crystals, similar to the previous study of $(La_{0.70}Ba_{0.3}MnO_3)_{1-x}/(Al_2O_3)_x$ [36]. Additional measurement of the magnetization curve ($M$–$H$) was performed to verify the magnetic behaviour for both samples at 300 K using a vibrating sample magnetometer (VSM). The result is presented in Figure 5. The S-shape curve's appearance for both samples indicates ferromagnetic behaviour [37]. The inset of Figure 5 shows an enlarged view in $M$–$H$ hysteresis loops, signifying the FM ordering of the samples [38]. The magnetization increased sharply at a low magnetic field for both samples; nonetheless, the value of saturation magnetization, $M_s$, increased from 1.81 $\mu_B$/f.u. to 4.11 $\mu_B$/f.u. for $x$ = 0 and $x$ = 0.04, respectively (Table 3). The rise in the $M_s$ value and electronic bandwidth, $W$, by $K^+$ substitution indicates the increasing overlapping of Mn-3d orbital ions with the O-2p orbital, thereby leading to the increase in effective FM interaction between Mn ions [9,31]. Moreover, the increasing Mn–O–Mn bond angle (listed in Table 1) possibly contributed to stronger FM, as highlighted in a previous study of $Nd_{0.7-x}La_xSr_{0.3}MnO_3$ [11]. Apart from that, the enhancement in magnetic properties can likewise arise from the enlargement of grain size with $K^+$ substitution. According to

Ibrahim et al. [39], compounds consisting of larger grain sizes with smaller grain boundaries exhibit a reduction in magnetic inhomogeneities, hence promoting the growth of the FM phase. On the other hand, the small value of coercivity, $H_{c,}$ is associated with the magnetic domains, which can be rotated easily in the direction of a magnetic field [32]. The obtained values of saturation magnetization, $M_s$, and coercivity, $H_c$, are listed in Table 3.

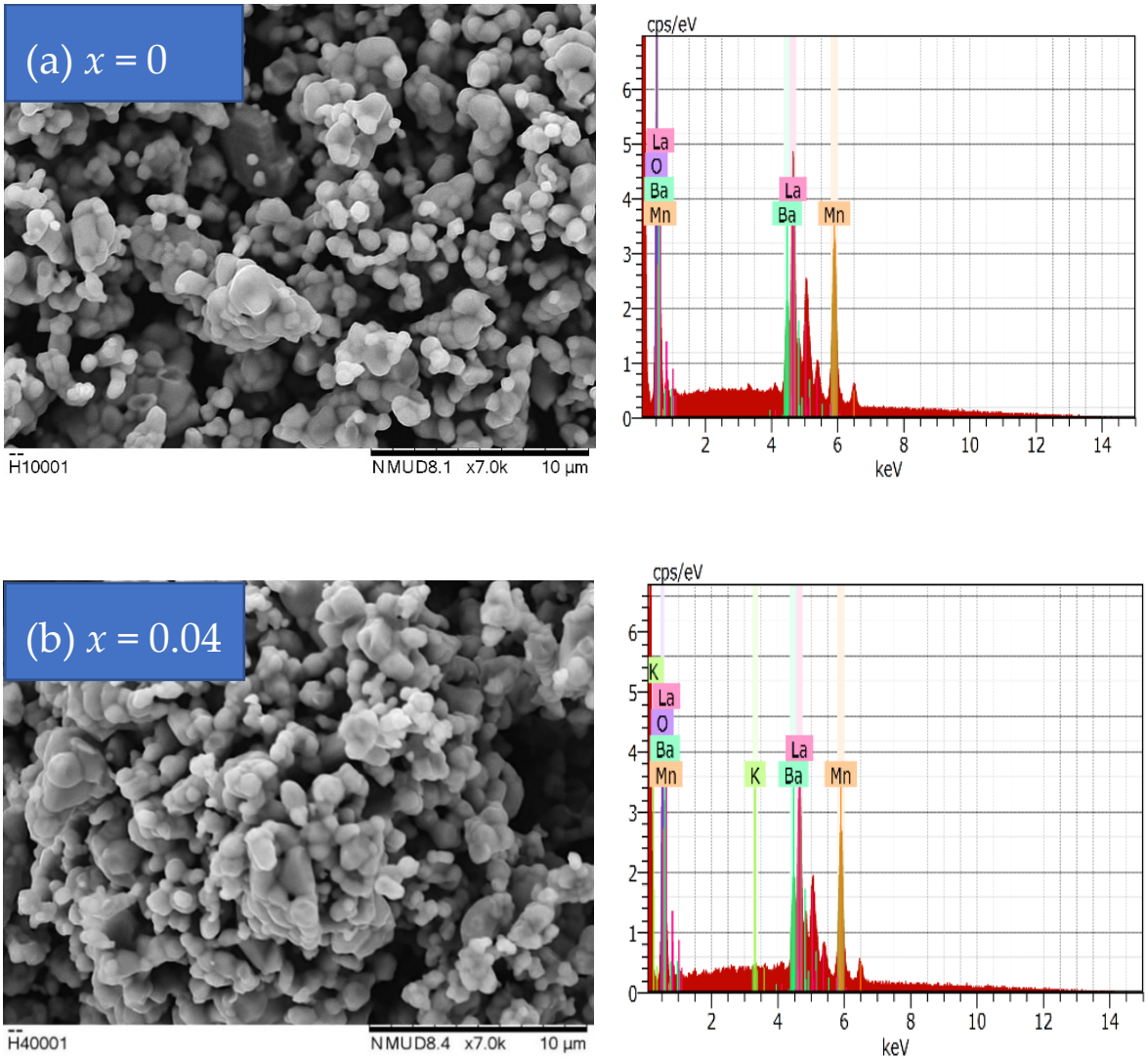


**Figure 3.** SEM-EDX analysis of $La_{0.7}Ba_{0.3-x}K_xMnO_3$ for (**a**) $x$= 0 and (**b**) $x$ = 0.04 samples.

**Table 2.** Atomic composition (%) of each element in $La_{0.7}Ba_{0.3-x}K_xMnO_3$ for ($x$= 0 and 0.04) samples obtained from EDX quantitative analysis.

| Sample | Atomic Composition (%) | |
|---|---|---|
| | $x$ = 0 | $x$ = 0.04 |
| La | 13.75 | 13.78 |
| Ba | 6.25 | 5.45 |
| K | 0 | 0.77 |
| Mn | 20.44 | 20.73 |
| O | 59.56 | 59.27 |
| Total | 100 | 100 |

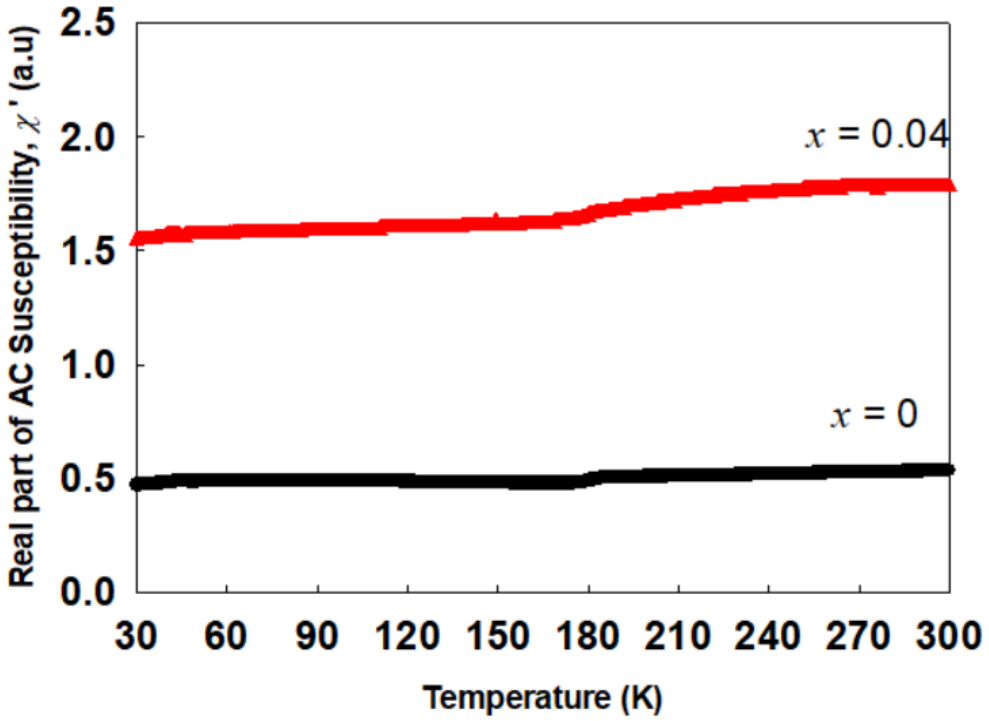


**Figure 4.** Temperature dependence of real part of AC susceptibility ($\chi'$) graph for $La_{0.7}Ba_{0.3-x}K_xMnO_3$ ($x$ = 0 and 0.04).

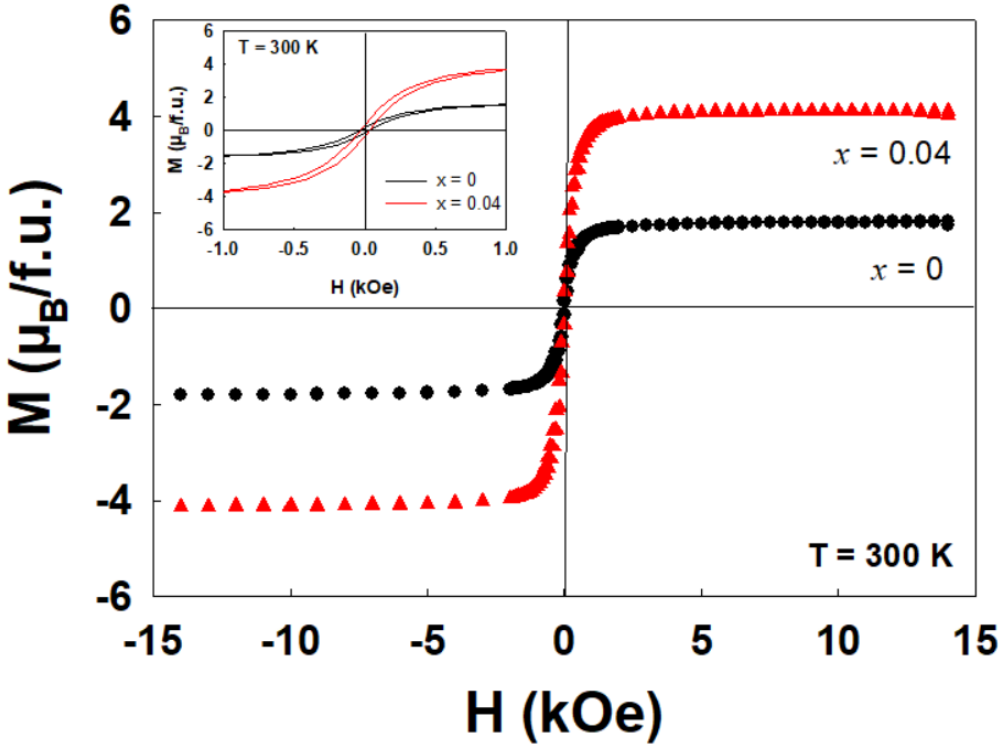


**Figure 5.** Magnetization, M, versus applied magnetic field, H, up to ±14 kOe for $La_{0.7}Ba_{0.3-x}K_xMnO_3$ ($x$ = 0 and 0.04). The inset shows the enlarged view of the M–H loop for the lower magnetic field.

**Table 3.** Magnetic parameters of $La_{0.7}Ba_{0.3-x}K_xMnO_3$ ($x$ = 0 and 0.04) obtained from VSM measurement.

| Sample | $x$ = 0 | $x$ = 0.04 |
|---|---|---|
| $M_s$ ($\mu_B$/f.u.) | 1.81 | 4.11 |
| $H_c$ (G) | 29.7 | 32.4 |

### 2.3. Electrical Properties

Figure 6 displays the temperature dependence of resistivity ($\rho$) data for $La_{0.7}Ba_{0.3-x}K_xMnO_3$ ($x$ = 0 and 0.04) at 0 T. Interestingly, the metal–insulator transition temperature, $T_{MI}$ increased from 257 K ($x$ = 0) to 271 K ($x$ = 0.04), while the peak value of resistivity decreased from 14.5 ohm.cm ($x$ = 0) to 0.08 ohm.cm ($x$ = 0.04). The reduction in $\rho$ could be attributed to the rise in the Mn–O–Mn bond angle (°) and increased bandwidth, W, with increasing $<r_A>$ (see Table 1). Based on Table 1, $K^+$ substitution increased the Mn–O–Mn bond angle and reduced the Mn–O bond length. This observed behaviour may facilitate the transfer of $e_g$ conduction electrons and enhance the delocalization of charge carriers. As a result, the electron mobility improves because the $e_g$ hopping process from $Mn^{3+}$ to $Mn^{4+}$ in the $Mn^{3+}$–$O^{2-}$–$Mn^{4+}$ double-exchange (DE) process is enhanced, leading to a reduction in resistivity. This is also evidenced by the increased bandwidth with $K^+$ (Table 1). The increasing value of W signifies that the overlapping between 3d-manganese and 2p-oxygen orbitals increased, thus favouring the transfer interaction of $e_g$ electrons between neighbouring Mn-sites [40]. Therefore, the strength of DE interaction in the $La_{0.7}Ba_{0.3-x}K_xMnO_3$ ($x$ = 0 and 0.04) system becomes stronger and $T_{MI}$ shifts to a higher temperature. Further, the reduction of grain boundaries effect may also contribute to the decrease in $\rho$. It can be seen that magnitude of $\rho$ is lowered by several orders ($10^{-2}$ Ω·cm) with $K^+$ substitution, which can be compared to the ceramic and single-crystal LCMO [41]. For granular systems, larger grain size may reduce the scattering at grain boundaries, which improves electron mobility and electrical conductivity [39,42]. Notably, the increase in grain size value and reduced grain boundaries for sample $x$ = 0.04 indicates the rise in the conduction channel for $e_g$ electrons' transfer to move between grains, which may also aid the DE process. These factors together may contribute to the significant decrease in resistivity. Similar findings were also discussed by Siwach et al. [43] and Huang et al. [41]. The obtained results are in good accordance with those interpreted in previous works [39,42].

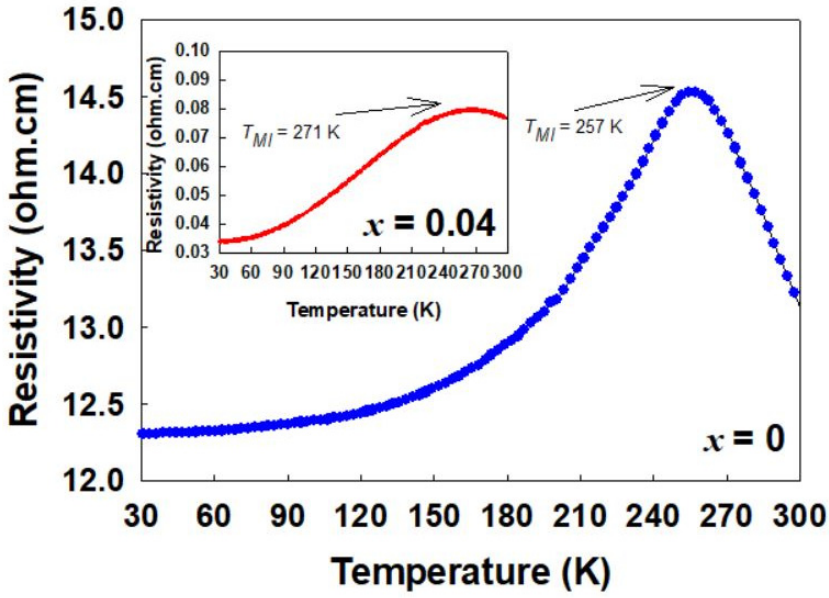


**Figure 6.** Temperature dependence of resistivity graph for $La_{0.7}Ba_{0.3-x}K_xMnO_3$ ($x$ = 0 and 0.04) under the absence of magnetic field.

Figure 7a,b shows the resistivity data for both samples with the absence and the presence of the magnetic field. At 0.8 T, resistivity for both samples is found to be decreased. This observed behaviour indicates the enhancement of delocalization related to the increased rate of $e_g$ itinerant hopping, alongside the improvement in charge carriers' mobility in the DE process [44–46]. The suppression of resistivity under the applied field could be interpreted by analyzing the influence of the magnetic field on the alignment of magnetic spins [30]. It is known that when the magnetic field is applied, the spin disorder is suppressed, and Mn spins within the disordered region realign along the field direction. Accordingly, more spins are ferromagnetically coupled, and the transfer of itinerant electrons in $Mn^{3+}$–$O^{2-}$–$Mn^{4+}$ is favoured, resulting in the improvement in electrical conductivity [17,21,44]. Nevertheless, the $T_{MI}$ for both samples remained unchanged upon applying an external magnetic field, in contrast with the previous report of $Nd_{0.6}Sr_{0.4-x}K_xMnO_3$ [9], where $T_{MI}$ slightly shifted to a higher temperature.

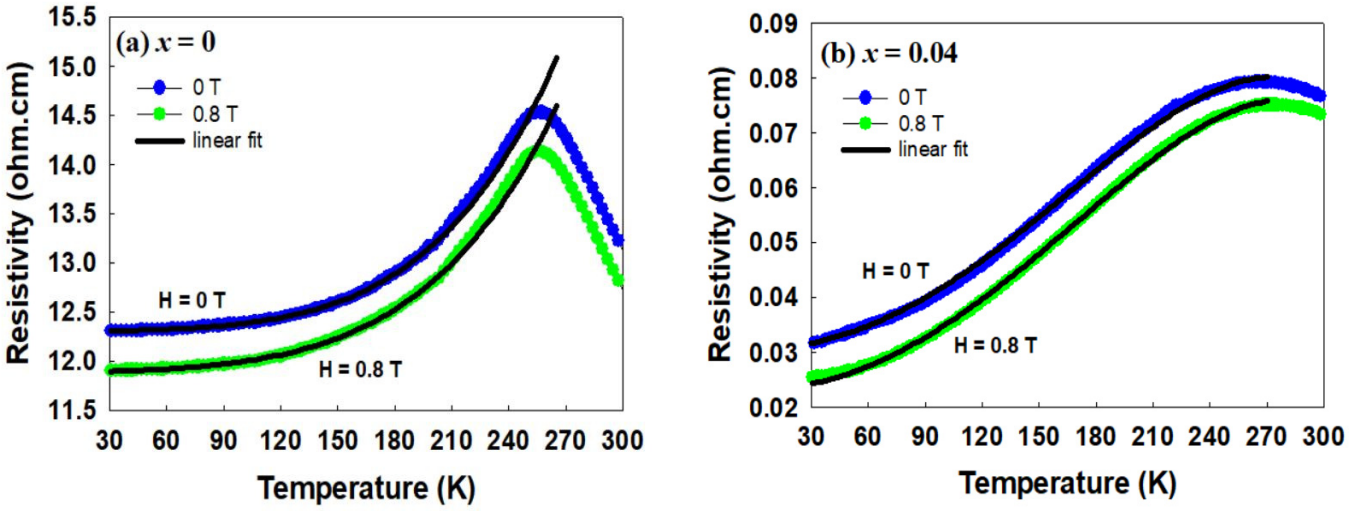


(**a**) (**b**)

**Figure 7.** Temperature dependence of resistivity graph for (**a**) $x = 0$ and (**b**) $x = 0.04$ in magnetic fields of 0 T and 0.8 T. The solid linear fit (black lines) corresponded to the fitting with Equation (4).

The temperature dependence of resistivity data can be divided into two regions: metallic ($T < T_{MI}$) and insulating region ($T > T_{MI}$), in which the nature of electrical conduction through the scattering process is more dominant in the former, while the hopping mechanism is more dominant in the latter [47]. In the metallic region ($T < T_{MI}$), the resistivity data for both samples at 0 $T$ and 0.8 $T$ were fitted according to the following equation [5,36,48]:

$$\rho = \rho_0 + \rho_2 T^2 + \rho_{4.5} T^{4.5} \quad (4)$$

where $\rho_0$ is the residual resistivity due to scattering by impurities, defects, grain boundaries, or domain walls; $\rho_2$ arises from electron–electron scattering; and $\rho_{4.5}$ is a resistivity factor due to electron–magnon scattering processes [5,36,48,49]. The data fit well and are of high quality with the square value of the linear correlation coefficient, $R^2$~99.9%. The related scattering parameters are listed in Table 4. Parameter $\rho_o$ yielded the highest value compared to $\rho_2$ and $\rho_{4.5}$ for both samples, indicating that the residual resistivity due to the grain boundary is more significant in the conduction process in the metallic region. It is also noticed that the residual resistivity decreases by more than two orders of magnitude. As evidenced in the XRD and SEM-EDX results, both investigated samples are well-crystallized. Thus, the contribution of impurities may not be responsible for such a reduction. This could be due to the additional influence of sample porosity, in addition to the grain boundary effect [30]. In the present study, the decreasing porosity with $K^+$ substitution may also increase the electron transport channels. As seen in Figure 3b, grains in the $K^+$-substituted

sample become more tightly packed, and hence the transfer of $e_g$ electrons between grains makes it easier to enhance the DE process [50]. Consequently, a drastic reduction in $\rho_o$ as well as resistivity in the K-substituted sample is observed (Figure 7a,b). On the other hand, the small value of $\rho_{4.5}$ could be attributed to the smaller spin inhomogeneity [30]. According to the increasing tolerance factor (Table 1), $K^+$ increases the stability of the perovskite system and possibly causes a decline in spin fluctuations. As reported by Sangeetha et al., the carrier scattering by thermal spin fluctuations plays an important role in the resistivity drop below $T_{MI}$ [51]. Since parameter $\rho_{4.5}$ represent the resistivity factor due to electron–magnon scattering, the substitution of non-magnetic $K^+$ possibly reduced the spin wave effect as well as spin fluctuations [52]; as a result, the value of $\rho_{4.5}$ decreased. A similar finding related to the obtained $-\rho_{4.5}$ value was also reported in the study of $La_{0.7-x}Y_xBa_{0.3}Mn_{1-x}Fe_xO_3$ [53], $La_{0.7-x}Bi_xSr_{0.3}MnO_3$ [52], and $La_{0.65-x}Bi_xCa_{0.35}MnO_3$ [48]. Based on Table 4, parameters $\rho_o$ and $\rho_2$ are reduced with $x$ due to the increase in grain size associated with the reduction in grain boundaries [30,42], which corresponded well to our SEM analysis result in Figure 3a,b.

**Table 4.** Best fit parameters for metallic region of $La_{0.7}Ba_{0.3-x}K_xMnO_3$ ($x$ = 0 and 0.04) using Equation (4).

| Sample, x | $\rho_o$ (Ω cm) | | $\rho_2$ (Ω cm/K$^{-2}$) | | $\rho_{4.5}$ (Ω cm/K$^{-4.5}$) | |
|---|---|---|---|---|---|---|
| | H = 0 T | H = 0.8 T | H = 0 T | H = 0.8 T | H = 0 T | H = 0.8 T |
| 0 | 12.30 | 11.89 | $4.92 \times 10^{-6}$ | $3.06 \times 10^{-6}$ | $3.01 \times 10^{-11}$ | $2.65 \times 10^{-11}$ |
| 0.04 | 0.03 | 0.02 | $1.19 \times 10^{-6}$ | $1.08 \times 10^{-6}$ | $-4.26 \times 10^{-13}$ | $-4.13 \times 10^{-13}$ |

Generally, all scattering parameters were observed to be reduced with $K^+$, evidencing that charge carriers experience less scattering and the rate of $e_g$ transfer between Mn ions in the DE process increases. The magnetic field application (0.8 T) further minimizes the scattering of charge carriers due to the parallel spin alignment of $e_g$ in the Mn–O–Mn network. Therefore, exchanges of interaction between Mn-sites increase and lead to the improvement in electrical conduction. Our result is consistent with the previous studies of electrical resistance in manganites under the influence of a magnetic field [44–46].

On the other hand, the conduction mechanism in the insulating region has been described through well-established hopping models: small polaron hopping (SPH) at $T > \theta_D/2$ ($\theta_D$ is Debye's temperature) and variable range hopping (VRH) at $T < \theta_D/2$. SPH is usually considered in the high-temperature insulating region, where thermal energy is sufficient to assist the hopping of charge carriers to their nearest neighbours with high mobility [21,54]. Small polaron hopping is expressed using the following equation [25]:

$$\rho = \rho_0 T \exp\left(E_a/k_B T\right) \quad (5)$$

where $E_a$ is the activation energy and $k_B$ is Boltzmann's constant. The values of $E_a$ for both samples are determined by the slope of ln ($\rho$/T) versus 1000/T curves, as shown in Figure 8a,b and the values are listed in Table 5. A reduction in $E_a$ was observed from 48.39 meV ($x$ = 0) to 40.07 meV ($x$ = 0.04), implying that $K^+$ enhanced the delocalization of $e_g$ electrons due to the reduction in grain-boundary effects and the widening of the $e_g$ electron bandwidth. As a result, the possibility of the conduction electron hopping to neighbouring sites was enhanced, thereby reducing the values of $E_a$. As the magnetic field is applied, the value of $E_a$ for both samples is further decreased. This behaviour signifies the weakening of attraction between lattice and electrons in the form of polarons, hence assisting the conductivity of $e_g$ carriers through the hopping process. The reduction in $E_a$ for both samples at 0.8 T is in agreement with the trend of decreasing resistivity observed in Figure 7a,b.

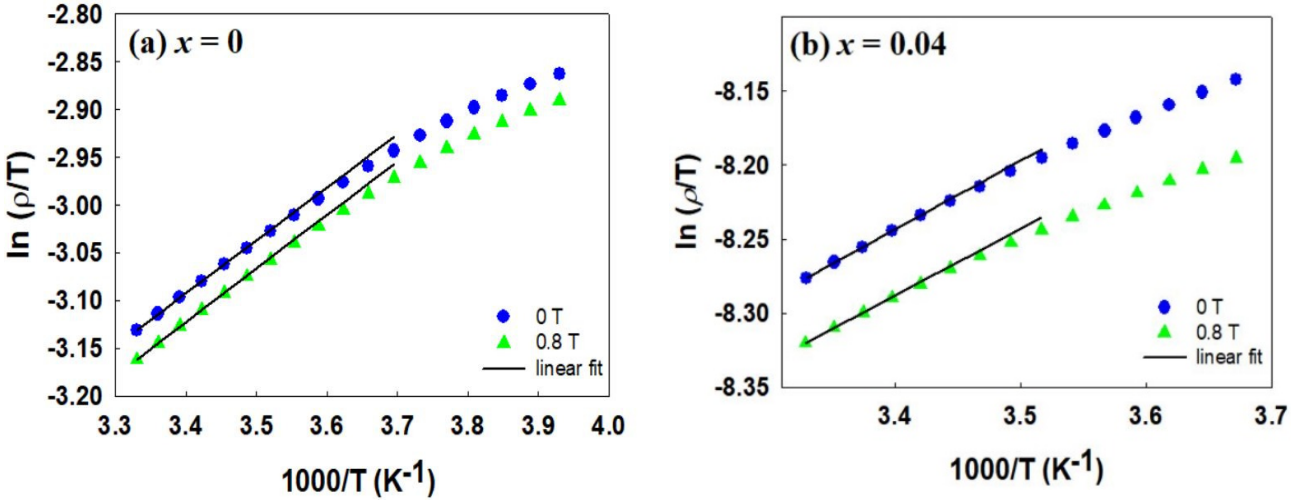


(**a**) (**b**)

**Figure 8.** The resistivity data fitting according to SPH model for (**a**) $x = 0$ and (**b**) $x = 0.04$.

**Table 5.** Fitting parameters of the experimental resistivity data for $La_{0.7}Ba_{0.3-x}K_xMnO_3$ ($x = 0$ and 0.04) according to SPH and VRH models. $E_a$ is the activation energy obtained in the SPH model; $T_{OM}$, $R_h$, $E_h$, and $N(E_F)$ correspond to the Mott's temperature, hopping distance, hopping energy, and charge carrier density of state (DOS) near the Fermi level in the VRH model, respectively.

| **Sample** | $x = 0$ | | $x = 0.04$ | |
|---|---|---|---|---|
| | **H = 0 T** | **H = 0.8 T** | **H = 0 T** | **H = 0.8 T** |
| | SPH model | | | |
| $E_a$ (meV) | 48.39 | 47.70 | 40.07 | 38.86 |
| | VRH model | | | |
| $T_{OM} \times 10^6$ (K) | 1.291 | 1.267 | 0.646 | 0.496 |
| $R_h$ (Å) | 13.93 | 13.86 | 11.71 | 10.97 |
| $E_h$ (meV) | 49.46 | 49.22 | 41.59 | 38.94 |
| $N(E_F)$ ($\times 10^{20}$) ($eV^{-1}$ $cm^{-3}$) | 1.774 | 1.810 | 3.550 | 4.620 |

Unlike the conduction mechanism described using the SPH model, the thermal energy is not large enough to allow electrons to hop to their nearest neighbours in a low-temperature insulating region. Therefore, it needs to hop further to find a site with a smaller potential difference [49,53]. In this case, variable range hopping (VRH) is more appropriate to illustrate the transport mechanism, which can be described by the following equation [55]:

$$\rho = \rho_{OM} \exp(T_{OM}/T)^{\frac{1}{4}} \quad (6)$$

where $\rho_{OM}$ is Mott's residual resistivity and $T_{OM}$ is Mott's temperature. $T_{OM}$ is obtained from the gradient of ln ($\rho$) versus $T^{1/4}$ plots (see Figure 9a,b), which can further be applied to determine the value of the charge carrier density of state (DOS) near the Fermi level $N(E_f)$, hopping energy $E_h$, and hopping distance $R_h$ [21,55]. Here, $\alpha$ and $k_B$ each represent the localization length at $\alpha = 4.5$ Å and Boltzmann's constant, respectively [55]. The linear fit using Equation (6) presents a straight line with $R^2$~99.9%, satisfying the VRH mechanism.

$$T_{OM} = 18 \,/\, \left(k_B N(E_F) \alpha^3\right) \quad (7)$$

$$R_h(T) = (3/8)\, \alpha\, (T_{OM}/T)^{\frac{1}{4}} \quad (8)$$

$$E_h(T) = (1/4) k_B\, T^{\frac{3}{4}}\, T_{OM}{}^{\frac{1}{4}} \quad (9)$$

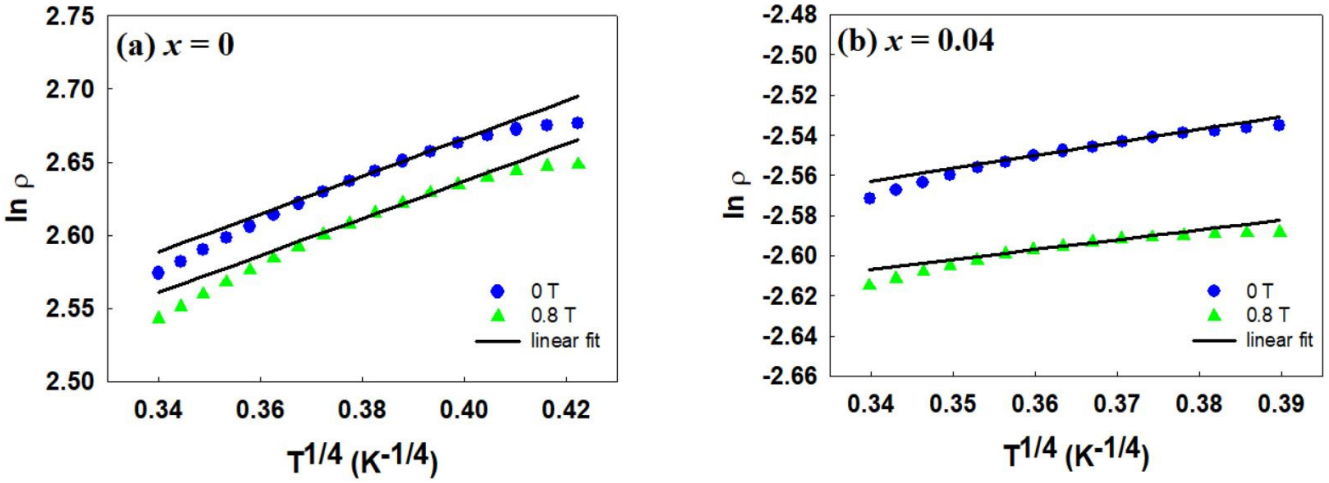


(**a**) (**b**)

**Figure 9.** The resistivity data fitting according to VRH model for (**a**) $x = 0$ and (**b**) $x = 0.04$.

The parameters related to the VRH model are listed in Table 5. It can be seen that the value of $T_{OM}$ decreases from $1.291 \times 10^6$ K ($x = 0$) to $0.646 \times 10^6$ K ($x = 0.04$) when $K^+$ is substituted into the compound. Moreover, one can observe that the values of $E_h$ and $R_h$ decrease with $K^+$ (Table 5), whereas the value of $N(E_F)$ increases. Such an increase in $N(E_F)$ reflects the increase in the density of states and the number of available hopping sites for the charge carriers. In the present study, it is suggested that $K^+$ substitution enhanced the interconnectivity between the grains as the grain size rose. Consequently, the hopping process becomes easier as the $e_g$ electron does not require large energy ($E_h$) to hop to a site beyond the nearest neighbour. The average hopping length is smaller than the average distance between the sites [53], and therefore, the hopping distance ($R_h$) decreased with $K^+$ substitution. Based on Table 5, both $R_h$ and $E_h$ were found to be decreased in the presence of a magnetic field, indicating the enhancement in delocalization while increasing the charge carrier density, $N(E_F)$, to enhance the hopping process and conductivity in the insulating region. These results agreed well with the reduction in resistivity observed in Figure 7a,b. Moreover, the obtained values of $N(E_F)$ were in the range of DOS at the Fermi level reported previously in other manganite systems [27,56,57].

### *2.4. Magnetoresistance (MR)*

Magnetoresistance (*MR*) is calculated by the following equation [9,58]:

$$MR\ (\%) = \frac{\rho\ (0,\ T) - \rho\ (H,\ T)}{\rho\ (0,\ T)} \times 100 \tag{10}$$

where $\rho(0)$ and $\rho(H)$ are the resistivity under zero magnetic field (0 T) and applied magnetic field (0.8 T), respectively. Figure 10 illustrates the temperature dependence of MR (%) under H = 0.8 T and its value at three respective temperatures; 30 K, $T_{MI,}$ and 300 K, which are tabulated in Table 6. MR has been previously discussed with respect to different contributions: intrinsic and extrinsic [28,42,44]. For the intrinsic MR effect, the spin ordering due to the suppression of spin fluctuations is responsible for explaining resistivity reduction under an applied magnetic field [13,28,42]. On the other hand, the extrinsic MR effect is explained based on spin-polarized tunnelling (SPT) related to the scattering of carriers at the grain boundaries. It is often discussed in polycrystalline granular systems [21,37,42,44]. As the electrons move between grains, they may encounter an insulating barrier consisting of disordered and scattered Mn spins, reducing connectivity among the grains. The application of a magnetic field may overcome the scattering effects [30,44]. As a result, the MR effect is observed at low temperatures. At 30 K, the MR (%) significantly increased

from 3.25% ($x$ = 0) to 25% ($x$ = 0.04). As discussed above, this behaviour could be ascribed to the influence of the extrinsic MR effect, whereby the SPT across grain boundaries is more dominant [37,58,59]. Grain boundaries acted as barriers to charge transport at zero field and restricted the tunnelling process due to disordered Mn spins [37]. In this study, a small substitution of $K^+$ possibly improved the spin alignment of the charge carrier at the grain boundaries region, and it was further enhanced with the application of a magnetic field. The realignment of disordered Mn spins in the grain boundary regions may reduce the magnetic disorder and facilitate the increase in intergrain SPT; thus, the MR effect is enhanced [30,58]. Meanwhile, the rise in MR (%) in the vicinity of $T_{MI}$ from 2.75% ($x$ = 0) to 5.31% ($x$ =0.04) possibly arose from the increase in the DE interactions as a result of the parallel alignment of spin at Mn–O–Mn couplings under magnetic field [30,58]. The similar behaviour of increased MR at $T_{MI}$ region due to enhanced DE has also been reported in $La_{0.65}Ca_{0.35-x}Li_xMnO_3$ [44] and $La_{0.5}Nd_{0.15}Ca_{0.25}A_{0.1}MnO_3$ (A = Ca, Li, Na, K) [60]. The highest MR (%) observed at 30 K for sample $x$ = 0.04 indicates that the extrinsic MR effect related to spin-polarized tunnelling is more pronounced in this system. For a small concentration of $K^+$ at $x$ = 0.04, the enhancement in the MR (%) value observed at 300 K from 3.01 % ($x$ = 0) to 4.24% ($x$ = 0.04) in a moderately low applied field gives this system a future prospect for advancement in room-temperature technological applications.

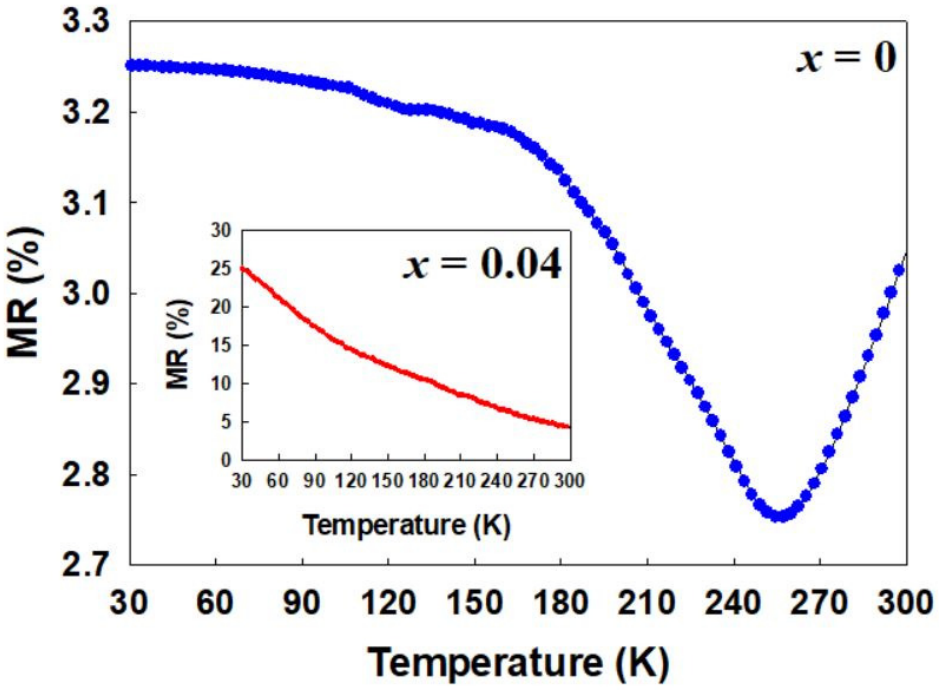


**Figure 10.** Temperature dependence of MR (%) for $La_{0.7}Ba_{0.3-x}K_xMnO_3$ ($x$ = 0 and 0.04) under H = 0.8 T.

**Table 6.** T MR (%) obtained for $La_{0.7}Ba_{0.3-x}K_xMnO_3$ ($x$ = 0 and 0.04) at three respective temperatures: 30 K, $T_{MI}$, and 300 K.

| Sample | MR (%) | | |
|---|---|---|---|
| | 30 K | $T_{MI}$ | 300 K |
| $x$ = 0 | 3.25 | 2.75 | 3.01 |
| $x$ = 0.04 | 25.0 | 5.31 | 4.24 |

In brief, $K^+$ substitution in the $La_{0.7}Ba_{0.3}MnO_3$ system enhanced the electrical conductivity and strengthened the magnetic interactions, which are suggested to be due to the improvement in microstructure, changes in bond angle, and increased hopping probability

of the $e_g$ conduction electrons. Since $K^+$ contributes to the rise of the MR effect, even under a low applied magnetic field, we believe that the present work is of considerable significance for the application of magnetic field sensors.

## 3. Materials and Methods

Polycrystalline samples of $La_{0.7}Ba_{0.3-x}K_xMnO_3$ ($x$ = 0 and 0.04) composition were synthesised via the solid-state method using $La_2O_3$, $BaCO_3$, $Mn_2O_3$, and $K_2CO_3$ as starting materials with 99.9% purity (Sigma-Aldrich). The powders were mixed and ground in an agate mortar for 1 h before the calcination process at 900 °C for 24 h. The processes of grinding and calcination were repeated twice to eliminate volatile foreign particles and carbon compounds in the samples [61]. After regrinding, the samples were pressed into pellets (13 mm diameter and 2.5 mm thickness) with an applied pressure of 5 tons using a hydraulic press, followed by a sintering process at 1100 °C for 24 h. The pellets were left to cool down to room temperature in the furnace before final grinding for 30 min for each sample. In addition, a slow cooling process at a rate of 1 °C/min was conducted after each calcination and sintering process to recover the oxygen lost at high temperature, thus maintaining the expected oxygen stoichiometry [37,62]. X-ray diffraction (XRD) was performed to examine the crystal structure of the sample using *PANalytical model Xpert PRO* with Cu Kα (λ = 1.5406 Å) radiation. The data were collected in the angle range of $2\theta = 10°–80°$ with a step size of 0.017° and further analysed through the Rietveld refinement method using the General Structure Analysis System (GSAS) and Graphical User Interfaces (EXPGUI) software programs. The grain morphology and the elemental analysis of the studied compounds were obtained via a scanning electron microscope (LEO model 982 Gemini) integrated with energy-dispersive X-ray spectroscopy (EDX). The electrical properties and magnetoresistance measurements were conducted using the standard four-probe technique in Janis model CCS-900T/204 cryostat at 30 K–300 K under zero field and applied field of 0.8 Tesla. Alternating Current (AC) susceptibility measurement was performed using Lakeshore AC susceptometer. The DC magnetic measurement was carried out using a Vibrating Sample Magnetometer (VSM, Lakeshore Model 7400) at 300 K under the magnetic fields of ±14 kOe.

## 4. Conclusions

In summary, the effects of $K^+$ substitution on the structural, magnetic, and electrical properties and magnetoresistance of $La_{0.7}Ba_{0.3-x}K_xMnO_3$ ($x$ = 0 and 0.04) perovskite manganites were investigated. Structural analysis revealed that both compounds exhibit a single-phase rhombohedral structure with the $R3\bar{c}$ space group. SEM analysis results showed that $K^+$ substitution leads to larger average grain sizes. Magnetization versus applied field ($M$–$H$) measurement demonstrated the strengthening of ferromagnetic (FM) interaction with $K^+$ substitution. Furthermore, electrical measurement displayed a reduction in resistivity and the metal–insulator transition temperature, $T_{MI}$ shifted to a higher temperature as $K^+$ was introduced into the system. The observed behaviour is correlated to the increasing tolerance factor ($\tau_G$) and bandwidth (W) with $K^+$ substitution, which increases the stability of the perovskite system and consequently enhances the mobility of charge carriers in the double-exchange (DE) mechanism. The grain boundary effects, which decreased as grain size increased for the K-substituted sample, play a significant role in the electrical conductivity behaviour. Suppression of resistivity for both samples was observed with the application of an external magnetic field of 0.8 T due to spin-ordering and improvement in the conduction process. Both samples exhibit metallic behaviour in the low-temperature region, which is well-fitted with the equation $\rho = \rho_0 + \rho_2 T^2 + \rho_{4.5} T^{4.5}$. Meanwhile, VRH and SPH models are used to elucidate the transport mechanism of both samples in the insulating region.

**Author Contributions:** Conceptualization, investigation, formal analysis, writing—original draft, A.Z.; investigation, formal analysis, N.A.A.; writing—review and editing, A.Z. and Z.M.; validation, N.I.; supervision, Z.M. All authors have read and agreed to the published version of the manuscript.

**Funding:** This work was financially supported by Universiti Teknologi MARA (UiTM) through the Young Talent Research Grant (YTRG), grant no. 600-RMC/YTR/5/3 (008/2020). The APC was funded by Research Management Centre, Universiti Teknologi MARA, UiTM, under Pembiayaan Yuran Penerbitan Artikel Berindeks (PYPA).

**Institutional Review Board Statement:** Not applicable.

**Informed Consent Statement:** Not applicable.

**Data Availability Statement:** Not applicable.

**Acknowledgments:** The authors would like to acknowledge the support and assistance from all lecturers and lab members of the Superconductor Lab, UiTM Shah Alam, throughout the study.

**Conflicts of Interest:** The authors declare no conflict of interest.

## References

1. Kumar, D.; Singh, A.K. Quenching of spin-orbit coupling and signature of Griffiths Phase in nanocrystalline $La_{0.6}Ba_{0.4}MnO_3$ perovskite manganite. *J. Solid State Chem.* **2022**, *309*, 122986. [CrossRef]
2. Dhahri, A.; Dhahri, J.; Dhahri, E. Effect of potassium doping on physical properties of perovskites $La_{0.8}Cd_{0.2-x}K_xMnO_3$. *J. Alloys Compd.* **2010**, *489*, 9–12. [CrossRef]
3. Das, S.; Dey, T.K. Magnetic entropy change in polycrystalline $La_{1-x}K_xMnO_3$ perovskites. *J. Alloys Compd.* **2007**, *440*, 30–35. [CrossRef]
4. Zaidi, A.; Alharbi, T.; Dhahri, J.; Alzobaidi, S.; Zaidi, M.A.; Hlil, E.K. $La_{0.67}Pb_{0.33-x}K_xMnO_3$ perovskites synthesized by sol–gel method: The effect of potassium substitution on the magnetic and electrical properties. *Appl. Phys. A Mater. Sci. Process.* **2017**, *123*, 94. [CrossRef]
5. Daivajna, M.D.; Rao, A.; Okram, G.S. Electrical, thermal and magnetic studies on Bi-substituted LSMO manganites. *J. Magn. Magn. Mater.* **2015**, *388*, 90–95. [CrossRef]
6. Koubaa, M.; Cheikhrouhou-Koubaa, W.; Cheikhrouhou, A. Effect of K doping on the physical properties of $La_{0.65}Ca_{0.35-x}K_xMnO_3$ ($0 \leq x \leq 0.2$) perovskite manganites. *J. Phys. Chem. Solids* **2009**, *70*, 326–333. [CrossRef]
7. Ma, F.; Jiao, Y.; Jiang, Z.; Du, A. Rhombohedral Lanthanum Manganite: A New Class of Dirac Half-Metal with Promising Potential in Spintronics. *ACS Appl. Mater. Interfaces* **2018**, *10*, 36088–36093. [CrossRef] [PubMed]
8. Zener, C. Interaction between the d-shells in the transition metals. II. Ferromagnetic compounds of manganese with Perovskite structure. *Phys. Rev.* **1951**, *82*, 403–405. [CrossRef]
9. Jeddi, M.; Massoudi, J.; Gharsallah, H.; Ahmed, S.I.; Dhahri, E.; Hlil, E.K. Impact of potassium substitution on structural, magnetic, magnetocaloric and magneto-transport properties of $Nd_{0.6}Sr_{0.4-x}K_xMnO_3$ ($0.0 \leq x \leq 0.2$) manganite. *J. Mater. Sci. Mater. Electron.* **2021**, *32*, 18751–18764. [CrossRef]
10. Thaljaoui, R.; Boujelben, W.; Pękała, M.; Pękała, K.; Fagnard, J.F.; Vanderbemden, P.; Donten, M.; Cheikhrouhou, A. Magnetocaloric effect of monovalent K doped manganites $Pr_{0.6}Sr_{0.4-x}K_xMnO_3$ ($x$ = 0 to 0.2). *J. Magn. Magn. Mater.* **2014**, *352*, 6–12. [CrossRef]
11. Vadnala, S.; Pal, P.; Asthana, S. Influence of A-site cation disorder on structural and magnetocaloric properties of $Nd_{0.7-x}La_xSr_{0.3}MnO_3$ ($x$ = 0.0, 0.1, 0.2 & 0.3). *J. Rare Earths* **2015**, *33*, 1072–1080.
12. Kalyana Lakshmi, Y.; Reddy, P.V. Influence of silver doping on the electrical and magnetic behavior of $La_{0.7}Ca_{0.3}MnO_3$ manganites. *Solid State Sci.* **2010**, *12*, 1731–1740. [CrossRef]
13. Zaidi, A.; Cherif, K.; Dhahri, J.; Hlil, E.K.; Zaidi, M.; Alharbi, T. Influence of Na-doping in $La_{0.67}Pb_{0.33-x}Na_xMnO_3$ ($0 \leq x \leq 0.15$) on its structural, magnetic and magneto-electrical properties. *J. Alloys Compd.* **2015**, *650*, 210–216. [CrossRef]
14. Cheikh-Rouhou Koubaa, W.; Koubaa, M.; Cheikhrouhou, A. Structural, magnetotransport, and magnetocaloric properties of $La_{0.7}Sr_{0.3-x}Ag_xMnO_3$ perovskite manganites. *J. Alloys Compd.* **2008**, *453*, 42–48. [CrossRef]
15. Regaieg, Y.; Koubaa, M.; Cheikhrouhou Koubaa, W.; Cheikhrouhou, A.; Sicard, L.; Ammar-Merah, S.; Herbst, F. Structure and magnetocaloric properties of $La_{0.8}Ag_{0.2-x}K_xMnO_3$ perovskite manganites. *Mater. Chem. Phys.* **2012**, *132*, 839–845. [CrossRef]
16. Razaq, D.S.; Kurniawan, B.; Munazat, D.R.; Watanabe, K.; Tanaka, H. Role of potassium substitution in the magnetic properties and magnetocaloric effect in $La_{0.8-x}K_xBa_{0.05}Sr_{0.15}MnO_3$ ($0 \leq x \leq 0.20$). *Crystals* **2020**, *10*, 407. [CrossRef]
17. Shaikh, M.W.; Varshney, D. Structural properties and electrical resistivity behaviour of $La_{1-x}K_xMnO_3$ ($x$ = 0.1, 0.125 and 0.15) manganites. *Mater. Chem. Phys.* **2012**, *134*, 886–898. [CrossRef]
18. Ben Rejeb, M.; Cheikhrouhou-Koubaa, W.; Koubaa, M.; Cheikhrouhou, A. Effect of Elaborating Method on Magnetic and Magnetocaloric Properties of $La_{0.65}Ca_{0.35-x}K_xMn0_3(0 \leq x \leq 0.2)$ Manganites. *J. Supercond. Nov. Magn.* **2015**, *28*, 839–846. [CrossRef]
19. Sdiri, N.; Jemai, R.; Bejar, M.; Hussein, M.; Khirouni, K.; Dhahri, E.; Mazen, S. Electrical conductivity and dielectric analysis of the perovskite $La_{0.7}Ca_{0.3-x}K_xMnO_3$ ($x$ = 0.00, 0.05 and 0.10). *Solid State Commun.* **2008**, *148*, 577–581. [CrossRef]
20. Ben Khlifa, H.; Regaieg, Y.; Cheikhrouhou-Koubaa, W.; Koubaa, M.; Cheikhrouhou, A. Structural, magnetic and magnetocaloric properties of K-doped $Pr_{0.8}Na_{0.2-x}K_xMnO_3$ manganites. *J. Alloys Compd.* **2015**, *650*, 676–683. [CrossRef]

21. Rozilah, R.; Ibrahim, N.; Mohamed, Z.; Yahya, A.K.; Khan, N.A.; Khan, M.N. Inducement of ferromagnetic-metallic phase in intermediate-doped charge-ordered $Pr_{0.75}Na_{0.25}MnO_3$ manganite by $K^+$ substitution. *Phys. B Condens. Matter.* **2017**, *521*, 281–294. [CrossRef]
22. Kumari, K.; Thakur, A.D.; Ray, S.J. The effect of graphene and reduced graphene oxide on the resistive switching behavior of $La_{0.7}Ba_{0.3}MnO_3$. *Mater. Today Commun.* **2021**, *26*, 102040. [CrossRef]
23. Esmaeili, S.; Ehsani, M.H.; Fazli, M. Structural, optical and photocatalytic properties of $La_{0.7}Ba_{0.3}MnO_3$ nanoparticles prepared by microwave method. *Chem. Phys.* **2020**, *529*, 110576. [CrossRef]
24. Mohamed, H.F.; Ahmed, A.M.; Diab, A.K.; Omar, E.Y. Impact of aluminum on the Seebeck coefficient and magnetic properties of $La_{0.7}Ba_{0.3}MnO_3$ manganites. *Chem. Phys. Lett.* **2019**, *726*, 22–28. [CrossRef]
25. Mohamed, A.E.M.A.; Mohamed, A.M.; ElShafaie, A.; Mohamed, H.F.; Diab, A.K.; Ahmed, A.M. Effect of NiO impurity on the magneto-transport properties of the $La_{0.7}Ba_{0.3}MnO_3$ granular manganite. *Chem. Phys. Lett.* **2018**, *713*, 272–276. [CrossRef]
26. Arbuzova, T.I.; Naumov, S.V. Magnetic polarons in doped $La_{0.7}Ca_{0.3}MnO_3$, $La_{0.7}Ba_{0.3}MnO_3$, and $La_{0.7}Sr_{0.3}MnO_3$ manganites. *JETP Lett.* **2015**, *101*, 760–764. [CrossRef]
27. Nguyen, L.H.; Dang, N.T.; Dang, N.V.; Bau, L.V.; Nam, P.H.; Phong, L.T.H.; Manh, D.H.; Phong, P.T. Structural, magnetic, and electrical properties of Ti-doped $La_{0.7}Ba_{0.3}Mn_{1-x}Ti_xO_3$ ($0 \leq x \leq 0.3$) ceramics. *J. Alloys Compd.* **2021**, *859*, 157831. [CrossRef]
28. Mohamed, A.E.M.A.; Hernando, B.; Díaz-García, M.E. Room temperature magneto-transport properties of $La_{0.7}Ba_{0.3}MnO_3$ manganite. *J. Alloys Compd.* **2017**, *695*, 2645–2651. [CrossRef]
29. Bally, M.A.A.; Ahsan, M.Z.; Islam, M.A.; Khan, F.A. Magnetic properties of $La_{0.55}Ca_xSr_{0.45-x}MnO_3$ perovskite manganite. *Results Phys.* **2021**, *21*, 103800. [CrossRef]
30. Lau, L.N.; Lim, K.P.; Ishak, A.N.; Kechik, M.M.A.; Chen, S.K.; Ibrahim, N.B.; Miryala, M.; Murakami, M.; Shaari, A.H. The physical properties of submicron and nano-grained $La_{0.7}Sr_{0.3}MnO_3$ and $Nd_{0.7}Sr_{0.3}MnO_3$ synthesised by sol–gel and solid-state reaction methods. *Coatings* **2021**, *11*, 361. [CrossRef]
31. Ahmed, S.A. Structural and electrical properties in $La_{1-x}Li_xMnO_3$. *J. Magn. Magn. Mater.* **2013**, *340*, 131–139. [CrossRef]
32. Messaoui, I.; Riahi, K.; Kumaresavanji, M.; Cheikhrouhou Koubaa, W.; Cheikhrouhou, A. Potassium doping induced changes of magnetic and magnetocaloric properties of $La_{0.78}Cd_{0.22-x}K_xMnO_3$ ($x$ = 0.00, 0.10, 0.15 and 0.20) manganites. *J. Magn. Magn. Mater.* **2018**, *446*, 108–117. [CrossRef]
33. Mtiraoui, N.; Dhahri, A.; Oumezine, M.; Dhahri, J.; Dhahri, E. Effects of nonmagnetic silver Ag doping on the structural, magnetic and electric properties in $La_{0.67}Pb_{0.33}MnO_3$ manganese oxides. *J. Magn. Magn. Mater.* **2011**, *323*, 2831–2836. [CrossRef]
34. Varshney, D.; Dodiya, N. Electrical resistivity of alkali metal doped manganites $La_xA_yMn_wO_3$ (A = Na, K, Rb): Role of electron-phonon, electron-electron and electron-magnon interactions. *Curr. Appl. Phys.* **2013**, *13*, 1188–1198. [CrossRef]
35. Mohamed, Z.; Sharon, I.S.; Ibrahim, N.; Maulud, M.F. Influence of Ruthenium Doping on the Crystal Structure and Magnetic Properties of $Pr_{0.67}Ba_{0.33}Mn_{1-x}Ru_xO_3$ Manganites. *Crystals* **2020**, *10*, 295. [CrossRef]
36. Ahmed, A.M.; Mohamed, H.F.; Diab, A.K.; Omar, E.Y. Crossover effect of magnetotransport and magnetocaloric effect in $(La_{0.7}Ba_{0.3}MnO_3)$ $1-x/(Al_2O_3)x$ composites. *J. Magn. Magn. Mater.* **2019**, *489*, 165388. [CrossRef]
37. Rozilah, R.; Ibrahim, N.; Yahya, A.K. Inducement of ferromagnetic–metallic phase and magnetoresistance behavior in charged ordered monovalent-doped $Pr_{0.75}Na_{0.25}MnO_3$ manganite by Ni substitution. *Solid State Sci.* **2019**, *87*, 64–80.
38. Kansara, S.B.; Dhruv, D.; Kataria, B.; Thaker, C.M.; Rayaprol, S.; Prajapat, C.L.; Singh, M.R.; Solanki, P.S.; Kuberkar, D.G.; Shah, N.A. Structural, transport and magnetic properties of monovalent doped $La_{1-x}Na_xMnO_3$ manganites. *Ceram. Int.* **2015**, *41*, 7162–7173. [CrossRef]
39. Ibrahim, N.; Rusop, N.A.M.; Rozilah, R.; Asmira, N.; Yahya, A.K. Effect of grain modification on electrical transport properties and electroresistance behavior of $Sm_{0.55}Sr_{0.45}MnO_3$. *Int. J. Eng. Technol.* **2018**, *7*, 113–117.
40. Soylu Koc, N.; Altintas, S.P.; Mahamdioua, N.; Terzioglu, C. Cation size mismatch effect in $(La_{1-y}RE_y)_{1.4}Ca_{1.6}Mn_2O_7$ perovskite manganites. *J. Alloys Compd.* **2019**, *797*, 471–476. [CrossRef]
41. Huang, Y.H.; Huang, K.F.; Luo, F.; He, L.L.; Wang, Z.M.; Liao, C.S.; Yan, C.H. Enhanced ferromagnetic transition and magnetoresistance in granular Ag-added $La_{0.7}Ca_{0.3}MnO_3$. *J. Solid State Chem.* **2003**, *174*, 257–263. [CrossRef]
42. Mohamed, H.F. Influence of sodium doping on the electrical and magnetic properties of $La_{0.90}Li_{0.10}MnO_3$ manganites. *J. Magn. Magn. Mater.* **2017**, *424*, 44–52. [CrossRef]
43. Siwach, P.K.; Prasad, R.; Gaur, A.; Singh, H.K.; Varma, G.D.; Srivastava, O.N. Microstructure-magnetotransport correlation in $La_{0.7}Ca_{0.3}MnO_3$. *J. Alloys Compd.* **2007**, *443*, 26–31. [CrossRef]
44. Verma, M.K.; Sharma, N.D.; Sharma, S.; Choudhary, N.; Singh, D. Structural and magneto-transport properties of Li-substituted $La_{0.65}Ca_{0.35-x}Li_xMnO_3$ ($0 \leq x \leq 0.15$) CMR manganites. *J. Alloys Compd.* **2020**, *814*, 152279. [CrossRef]
45. Tripathi, R.; Awana, V.P.S.; Kishan, H.; Balamurugan, S.; Bhalla, G.L. Impact of silver addition on room temperature magneto-resistance in $La_{0.7}Ba_{0.3}MnO_3$ (LBMO): $Ag_x$ ($x$ = 0.0, 0.1, 0.2, 0.3, 0.4). *J. Supercond. Nov. Magn.* **2008**, *21*, 151–159. [CrossRef]
46. Mansuri, I.; Varshney, D. Structure and electrical resistivity of $La_{1-x}Ba_xMnO_3$ ($0.25 \leq x \leq 0.35$) perovskites. *J. Alloys Compd.* **2012**, *513*, 256–265. [CrossRef]
47. Pal, A.; Rao, A.; Kekuda, D.; Nagaraja, B.S.; Mondal, R.; Biswas, D. Investigation of cationic disorder effects on the transport and magnetic properties of perovskite $Pr_{0.7-x}RE_xSr_{0.3}MnO_3$ ($x$ = 0.0, 0.2; RE = Nd, Sm & Gd). *J. Magn. Magn. Mater.* **2020**, *512*, 167011.
48. Manjunatha, S.O.; Rao, A.; Poornesh, P.; Lin, W.J.; Kuo, Y.K. Magnetic inhomogeneity and Griffiths phase in Bi substituted $La_{0.65-x}Bi_xCa_{0.35}MnO_3$ manganites. *Phys. B Condens. Matter.* **2016**, *498*, 82–91. [CrossRef]

49. Ibrahim, N.; Rozilah, R.; Mohamed, Z.; Yahya, A.K. Magnetic and electronic transport properties of electron-doped $La_{0.9-x}Bi_xTe_{0.1}MnO_3$ ($0.00 \leq x \leq 0.2$) Manganites. *Mater. Chem. Phys.* **2020**, *248*, 122940. [CrossRef]
50. Yadav, A.; Shah, J.; Gupta, R.; Shukla, A.; Singh, S.; Kotnala, R.K. Role of spin-glass phase for magnetoresistance enhancement in nickel substituted lanthanum calcium manganite. *Ceram. Int.* **2016**, *42*, 12630–12638. [CrossRef]
51. Sangeetha, M.; Babu, V.H. Effect of yttrium substitution on the electrical and magnetic properties of $La_{0.7}Ba_{0.3}MnO_3$ compound. *J. Magn. Magn. Mater.* **2015**, *389*, 5–9. [CrossRef]
52. Daivajna, M.D.; Rao, A.; Okram, G.S. Electrical, thermal and magnetic properties of Bi doped La $_{0.7-x}Bi_xSr_{0.3}MnO_3$ manganites. *J. Alloys Compd.* **2014**, *617*, 345–351. [CrossRef]
53. Ben Abdelkhalek, S.; Kallel, N.; Kallel, S.; Guizouarn, T.; Peña, O.; Oumezzine, M. Transport behavior and mechanism of conduction of simultaneously substituted y and Fe in $La_{0.7}Ba_{0.3}MnO_3$ perovskite. *Phys. B Condens. Matter* **2011**, *406*, 4060–4067. [CrossRef]
54. Khan, M.H.; Roychowdhury, A.; Das, D.; Pal, S. Adiabatic polaron hopping conduction and Griffiths phase in electron-doped $Ca_{0.85}Dy_{0.15}MnO_3$. *J. Alloys Compd.* **2015**, *650*, 328–335. [CrossRef]
55. Saleh, J.A.; Sarsari, I.A.; Kameli, P.; Salamati, H. Influence of Al-doping on the structural, magnetic, and electrical properties of $La_{0.8}Ba_{0.2}Mn_{1-x}Al_xO_3$ ($0 \leq x \leq 0.25$) manganites. *J. Magn. Magn. Mater.* **2018**, *465*, 339–347. [CrossRef]
56. Venkataiah, G.; Krishna, D.C.; Vithal, M.; Rao, S.S.; Bhat, S.V.; Prasad, V.; Subramanyam, S.V.; Reddy, P.V. Effect of sintering temperature on electrical transport properties of $La_{0.67}Ca_{0.33}MnO_3$. *Phys. B Condens. Matter* **2005**, *357*, 370–379. [CrossRef]
57. Manjunatha, S.O.; Rao, A.; Awana, V.P.S.; Okram, G.S. Investigation on magnetic, electrical and thermoelectric power of Bi-substituted $La_{0.8}Ca_{0.2}MnO_3$ manganites. *J. Magn. Magn. Mater.* **2015**, *394*, 130–137. [CrossRef]
58. Asmira, N.; Ibrahim, N.; Mohamed, Z.; Yahya, A.K. Effect of $Cr^{3+}$ substitution at Mn-site on electrical and magnetic properties of charge ordered $Bi_{0.3}Pr_{0.3}Ca_{0.4}MnO_3$ manganites. *Phys. B Condens. Matter* **2018**, *544*, 34–46. [CrossRef]
59. Ghani, M.A.; Supardan, S.N.; Yahya, A.K. Effect of Bi Substitution on Transport and Magnetoresistance Properties of Electron-Doped $La_{0.7-x}Bi_xCe_{0.3}MnO_3$ Ceramics. *J. Supercond. Nov. Magn.* **2015**, *28*, 1835–1841. [CrossRef]
60. Kumar Verma, M.; Dutt Sharma, N.; Sharma, S.; Choudhary, N.; Singh, D. High magnetoresistance in $La_{0.5}Nd_{0.15}Ca_{0.25}A_{0.1}MnO_3$ (A = Ca, Li, Na, K) CMR manganites: Correlation between their magnetic and electrical properties. *Mater. Res. Bull.* **2020**, *125*, 110813. [CrossRef]
61. Mendonca, L.D.; D'Souza, A.; Murari, M.S.; Daivajna, M.D. Magneto Transport Anomaly of Bismuth Substituted (La, Na) $MnO_3$. *J. Supercond. Nov. Magn.* **2020**, *33*, 1809–1819. [CrossRef]
62. Trukhanov, S.V.; Kasper, N.V.; Troyanchuk, I.O.; Tovar, M.; Szymczak, H.; Bärner, K. Evolution of magnetic state in the $La_{1-x}Ca_xMnO_{3-\gamma}$ ($x$ = 0.30, 0.50) manganites depending on the oxygen content. *J. Solid State Chem.* **2002**, *169*, 85–95. [CrossRef]